SUPPLEMENTARY INFORMATION AND METHODS

**Biostratigraphy, Paleontology and Age**
There has been considerable study on the Shangsi section, as it was once regarded as a candidate for the PTB global stratotype section and point (GSSP). The base-Triassic (base-Induan) GSSP has been decided at Meishan. The section has been described in terms of bed numbers (Lai et al., 1996; Nicoll et al., 2002; Jiang et al., 2011) and we follow the terminology, but it is difficult to be precise given potential differences in measurements and lithologic depiction. Based on thickness measurements our bedding plane would be within the lower part of bed 29a, but compared in terms of lithology to the section depicted in Jiang et al. (2011) our bedding plane would be at the very top of bed 28d and our overlying *Claraia* bed would be the base of Bed 29a. Regardless, our bed falls within the *Clarkina taylorae* Zone, which is typically correlated with the *Hindeodus parvus* Zone (Yuan et al., 2014). Nicoll et al. (2002) suggested that *H. parvus* was diachronous compared to other South China sections as they recovered the first occurrence in Bed 30, 4 metres above the extinction horizon (top of bed 26). Jiang et al. (2011) recovered *H. parvus* lower within Bed 29c and here we report it at the top of Bed 28d, which is entirely predictable with increased sampling. We recovered *H. parvus*, *H. praeparvus*, *H. eurypyge*, *Clarkina* sp. and *Ellisonia* sp. This confirms the earliest Triassic *Hindeodus parvus* Zone age correlation for our study. In addition, the high-precision geochronology by Shen et al. (2011) also supports the PTB position and a relatively higher position of the FO of *Hindeodus parvus* at Shangsi than at Meishan. Bed 28d top interpolates to ~251.89 Ma, ~10 kyrs into the Triassic and ~50 kyrs after the initial extinction, based on ages of 251.941 +/- 0.037 Ma for the extinction, 251.902 +/- 0.024 Ma for the PTB, and 251.880 +/- 0.031 for *Isarcica staechei* Zone (Burgess et al., 2014).

Fossil taxa exposed along the upper surface of Bed 28d include one cidaroid echinoid species, one ammonoid species (tentatively assigned to *Otoceras* sp. cf. *boreale*), five bivalve species (morphospecies) and one type of domnichnia trace fossil (*Cylindrichnus*?). Lawrence (2013) and Siikavuopio et al. (2008) discuss ecologic requirements of sea urchins (echinoids); also see many references in Song et al. (2014). The echinoids are compared to *Eotiaris* sp. (Thompson et al., 2015). The bivalves were not sufficiently studied to expose umbonal and auricular structures necessary for specific identification, but most specimens differ from those in Bed 29a, which are dominated by *Claraia wangi*. The trace fossil is lined and likely a filter feeder at the sediment-water interface indicating an oxygenated sea floor during Bed 28d deposition. These taxa took refuge is this deeper water site away from increasing water temperatures as also reported by Zhang et al., 2015. and Song et al., 2014.

**Lithology**
The underlying Permian Bed 22 includes a pelagic fauna dominated by nautiloids, ammonoids, and radiolarian with only two benthic fossils (one bivalve and one brachiopod) in two m$^2$ quadrats (Figs. DR1 and DR3A). Above the extinction level the lithology is dominated by soft shale lacking microbialite laminae, but including rare specimens of *Claraia*. Bed 28d stands in

contrast as a strongly lithified muddy limestone interlaminated with wrinkled microbial laminae (Figs. DR1 and DR2) and zones of fenestral fabric filled with calcite cement (Fig. DR1). Either the section had shallowed to the photic zone or water clarity increased. Immediately overlying as bed 29a is a thin unit of shale and volcanic ash with abundant thin-shelled *Claraia* forming what appear to be thin calcareous laminae (DR1). Microbial laminae occur higher in the section, but additional occurrences of echinoids have not been found.
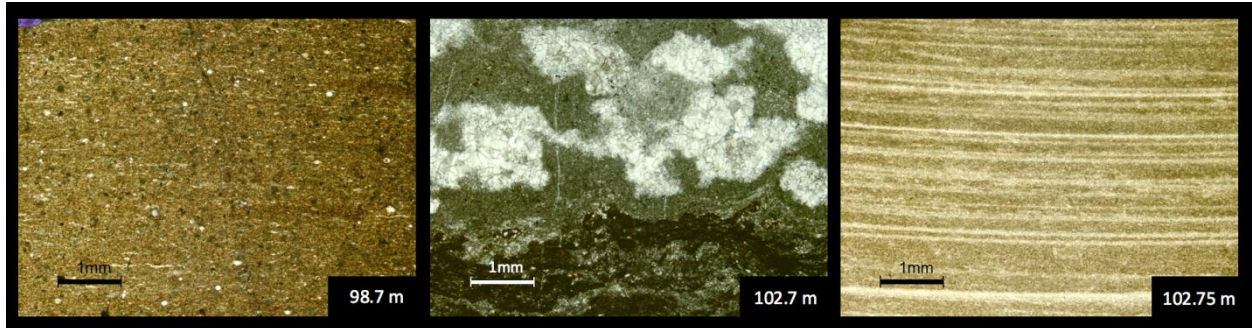


Figure DR1. (Left) Thin-section image of Bed 22, composed of a siliceous radiolarian mudstone to wackestone, deposited during the Late Permian. (Middle) Thin-section image of Bed 28d, composed of a calcimicrobial limestone, deposited during the Griesbachian. The open-spaced structures filled with calcite represent fenestral fabric. A microbial laminated surface is visible in the bottom half of the image. (Right) Thin-section image of the overlying shale with *Claraia* in Bed 29a.
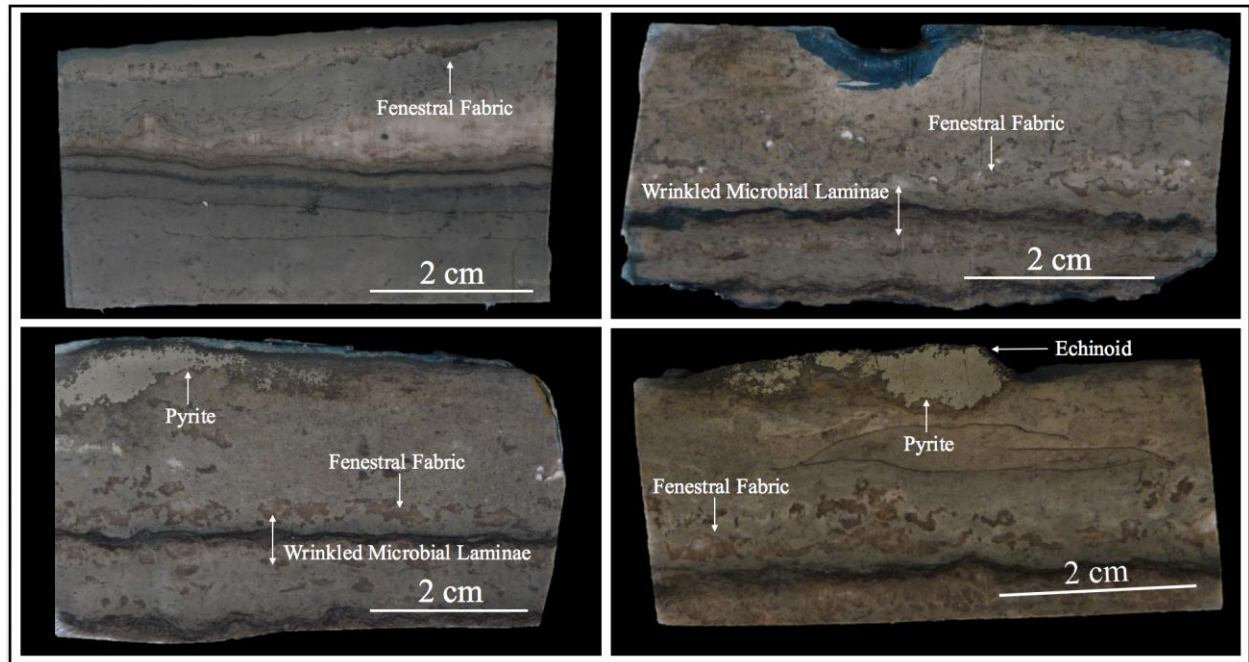


Figure DR2. Four images of polished slabs of the upper part of Bed 28d at 102.7 m that display alternating wrinkled microbial laminae and fenestral fabric. The two lower specimens show blocky diagenetic pyrite that here occurs immediately below echinoid specimens.
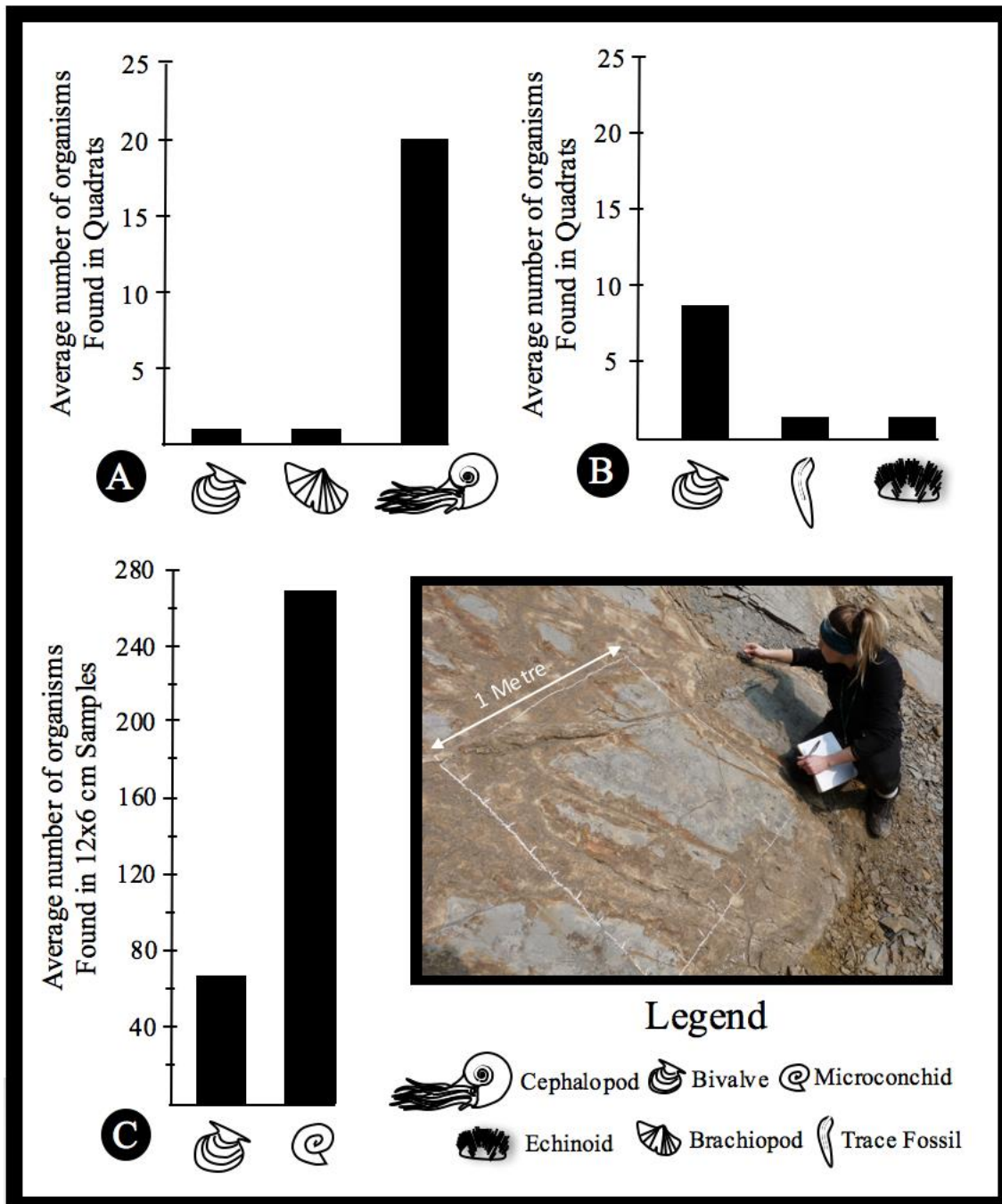
Figure DR3. Graph A. Average number of individual specimens of each taxon found within the quadrats on Bed 22, deposited during the latest Permian. A total of two quadrats were drawn on this bedding surface. Graph B. Average number of individual specimens of each taxon found within the quadrats on Bed 28d, deposited during the Griesbachian. A total of eight quadrats were drawn on this bedding surface (see Fig. DR5). Graph C. Average number of individual specimens of each taxon found within a 12x6 cm sample taken from the shaly unit of basal Bed 29a, deposited during the Early Triassic; seven samples were examined to calculate the average population density.
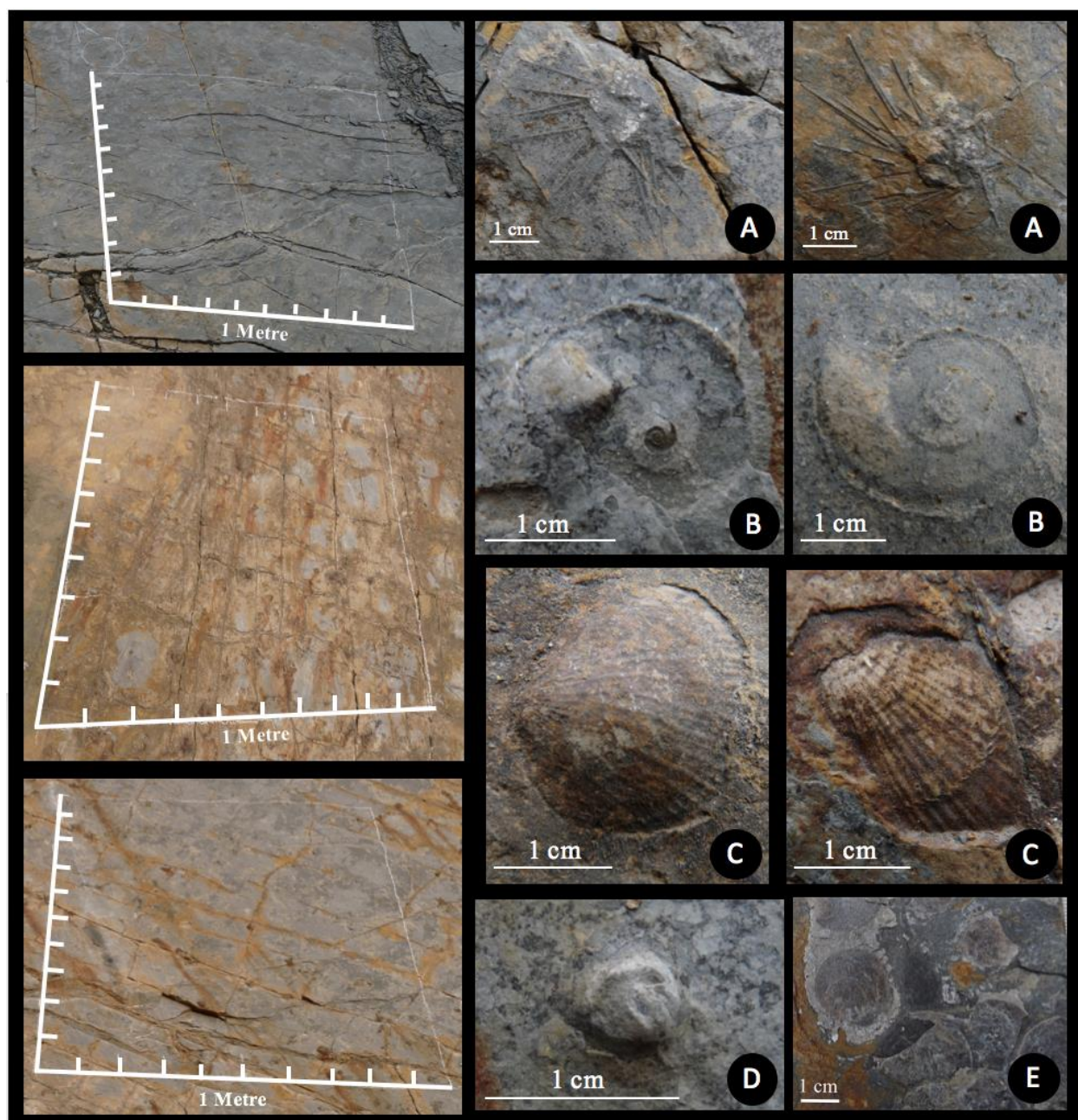
Figure DR4: (Left) Three quadrats that were drawn with white chalk on Bed 28d. (Right) Photographs of various taxa found on bed 29, showing preservation quality. (A) Echinoids are compared to *Eotiaris* sp. (B) Ammonoids tentatively compared to *Otoceras* cf. *boreale*. (C) Bivalves. (D) upper view of *Cylindrichnus*? trace fossil (see Fig. 2D for thin-section cross-section). (E) *Claraia* found within the shale of basal Bed 29a.

Figure DR5. Annotated photograph showing the quadrats and the distribution of echinoids. A total of 40 echinoids were observed and recorded along this bedding surface. The dashed line shows the limit of our mapping of the Bed 28d surface.

**Geochemistry**

Geochemical samples (n = 10) were cleaned in ethanol in an ultrasonic bath, followed by rinsing with deionized water. Dried samples were powdered using an agate mill. Trace elements were measured in powdered samples using a Niton XL3t handheld XRF analyzer. Each sample was measured for 160 seconds using the TestAllGeo procedure, with the measurement repeated three times to assess repeatability. Stable isotopes were measured at the University of Calgary Isotope Science Laboratory (ISL), Organic carbon and nitrogen were measured on a Thermo Finnigan Delta V isotope ratio mass spectrometer (IRMS) connected to an Elementar Cube elemental analyzer, and corrected to USGS glutamic acid standards 40 ($\delta^{13}C = \delta 26.39$ ‰; $\delta^{15}N = \delta 4.52$ ‰) and 41 ($\delta^{13}C = 37.63$ ‰; $\delta^{15}N = 47.57$ ‰). Organic carbon isotope sample powders were treated with 10% HCl prior to analysis to remove carbonate. Total organic carbon was determined during organic carbon measurements, and corrected for carbonate content. Isotopes of carbonate were measured using a Thermo Finnigan Delta V IRMS with Gasbench peripheral. Measurements were corrected using internal laboratory standards. All data are reported in Supplementary Table DR1 below.
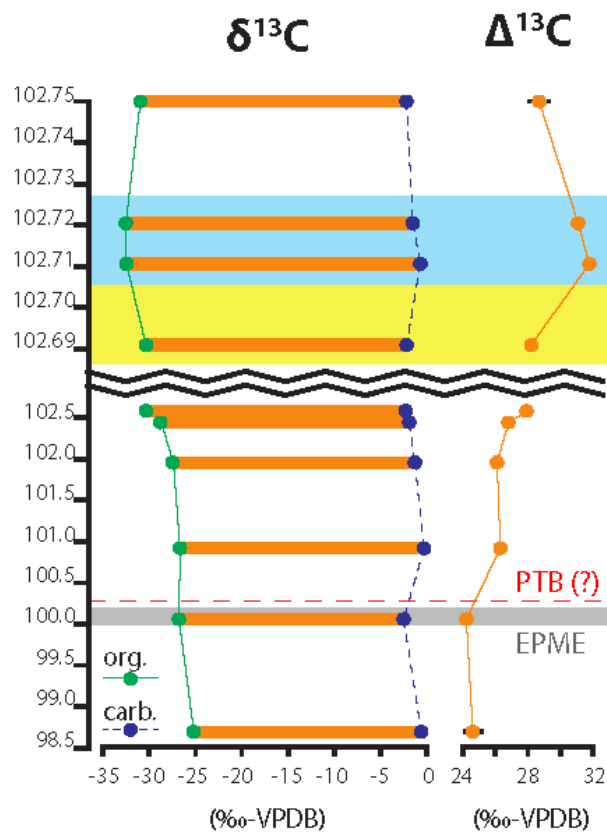
Figure DR6. Stratigraphic trends in organic and inorganic carbon isotopes, and the photosynthetic fractionation effect ($\Delta^{13}$C). Yellow highlighted interval is the echinoid-dominated assemblage (Bed 28d). Blue highlighted interval corresponds to the *Claraia*-dominated assemblage (Bed 29a). Note the expanded scale above 102.5 m.

| | height (m) | Mo | ± | U | ± | Th | ± | Sc | ± | Th/Sc | ± | P | ± | TOC (%) | Carb. | $\delta^{13}C_{org}$ | σ | $\delta^{13}C_{carb}$ | σ | $\Delta^{13}C$ | ± | $\delta^{15}N$ | σ |
|---|---|---|---|---|---|---|---|---|---|---|---|---|---|---|---|---|---|---|---|---|---|---|---|
| SHR1 | 98.70 | 1.7 | 1.0 | 4.9 | 1.9 | 3.6 | 1.1 | 43.5 | 17.4 | 0.1 | 0.0 | 969.9 | 195.7 | 0.11 | 9% | -25.2 | 0.6 | -0.6 | – | 24.6 | 0.6 | 0.5 | 0.2 |
| SHR2 | 100.08 | 2.0 | 1.3 | 9.4 | 2.9 | 17.0 | 1.6 | 83.4 | 25.7 | 0.2 | 0.1 | 335.8 | 160.4 | 0.20 | 21% | -26.8 | 0.1 | -2.5 | – | 24.2 | 0.1 | 1.4 | 0.2 |
| SHR3 | 100.95 | 0.4 | 1.3 | 9.7 | 2.8 | 14.0 | 1.5 | 229.3 | 37.6 | 0.1 | 0.0 | 432.1 | 164.1 | 0.14 | 30% | -26.7 | 0.1 | -0.3 | – | 26.3 | 0.1 | 1.4 | 0.3 |
| SHR4 | 102.00 | 0.0 | 1.2 | 10.2 | 2.8 | 12.8 | 1.5 | 204.7 | 37.0 | 0.1 | 0.0 | 95.0 | 205.7 | 0.22 | 29% | -27.4 | 0.1 | -1.3 | – | 26.1 | 0.1 | 1.2 | 0.3 |
| SHR5 | 102.49 | 0.2 | 1.3 | 0.6 | 2.7 | 4.8 | 1.4 | 397.4 | 103.4 | 0.0 | 0.0 | 0.0 | 150.6 | 0.06 | 83% | -28.7 | 0.1 | -1.9 | – | 26.8 | 0.1 | 0.9 | 0.2 |
| SHR6 | 102.63 | 2.7 | 0.9 | 0.6 | 2.6 | 3.6 | 1.4 | 240.2 | 117.0 | 0.0 | 0.0 | 0.0 | 148.5 | 0.10 | 88% | -30.3 | – | -2.3 | – | 28.0 | 0.0 | 0.1 | 0.6 |
| SHR7 | 102.69 | 6.8 | 1.0 | 0.0 | 2.9 | 5.5 | 1.5 | 283.9 | 104.7 | 0.0 | 0.0 | 0.0 | 165.9 | 0.12 | 77% | -30.4 | 0.1 | -2.2 | 0.02 | 28.2 | 0.1 | 0.5 | 1.6 |
| SHR8 | 102.71 | 3.7 | 1.3 | 13.6 | 2.8 | 14.2 | 1.6 | 30.0 | 19.0 | 0.5 | 0.3 | 1573.3 | 166.5 | 2.37 | 17% | -32.5 | 0.2 | -0.7 | – | 31.8 | 0.2 | 0.6 | 0.0 |
| SHR9 | 102.72 | 10.0 | 1.4 | 10.8 | 2.8 | 15.4 | 1.6 | 42.5 | 21.5 | 0.4 | 0.2 | 1163.3 | 185.6 | 1.90 | 14% | -32.5 | 0.1 | -1.5 | – | 31.1 | 0.1 | 0.5 | 0.3 |
| SHR10 | 102.75 | 8.9 | 1.2 | 4.4 | 2.9 | 8.0 | 1.5 | 309.5 | 78.9 | 0.0 | 0.0 | 0.0 | 255.0 | 0.41 | 59% | -31.0 | 0.7 | -2.2 | – | 28.7 | 0.7 | -0.4 | 0.7 |

Table DR1: Summary of geochemical data from the Shangsi section; σ = standard deviation of repeat measurements, ± = standard error.

**References**

Burgess, S.D., Bowring, S., and Shen, S.Z., 2014, High-precision timeline for Earth's most severe extinction: Proceedings of the National Academy of Sciences of the United States of America, v. 111, p. 3316-3321, doi:10.1073/pnas.1317692111 (correction available at http://dx.doi.org/10.1073/pnas.1403228111).

Jiang, H.S., Joachimski, M.M., Wignall, P.B., Zhang, M. and Lai, X.L., 2015, A delayed end-Permian extinction in deep-water locations and its relationship to temperature trends (Bianyang, Guizhou Province, South China: Palaeogeography, Palaeoclimatology, Palaeoecology, v. 440, p. 690-695.

Jiang, H.S., Lai, X.L., Yan, C.B., Aldridge, R.J., Wignall, P.W., and Sun, Y.D., 2011, Revised conodont zonation and conodont evolution across the Permian–Triassic boundary at the Shangsi section, Guangyuan, Sichuan, South China: Global and Planetary Change, v. 77, p. 103-115, doi:10.1016/j.gloplacha.2011.04.003.

Lai, X.L., Yang, F., Hallam, A., and Wignall, P.B., 1996, The Shangsi section, candidate of the Global Stratotype Section and Point of the Permian-Triassic Boundary: in The Paleozoic-Mesozoic Boundary Candidates of Global Stratotype Section and Point of the Permian-Triassic Boundary, (ed. Yin, H.F.), China University of Geosciences Press, Wuhan, p. 113-124.

Lawrence, J.M., 2013, Sea urchins: Biology and ecology v. 38: London, Elsevier, Academic Press, 550 pp.

Nicoll, R.S., Metcalfe, I., and Cheng-Yuan, W., 2002, New species of the conodont Genus *Hindeodus* and the conodont biostratigraphy of the Permian–Triassic boundary interval: Journal of Asian Earth Sciences, v. 20, p. 609-631, doi:10.1016/S1367-9120(02)00021-4.

Siikavuopio, S.I., Mortensen, A., and Christiansen, J.S., 2008, Effects of body weight and temperature on feed intake, gonad growth and oxygen consumption in green sea urchin, *Strongylocentrotus droebachiensis*: Aquaculture (Amsterdam, Netherlands), v. 281, p. 77-82, doi:10.1016/j.aquaculture.2008.05.033.

Song, H., Wignall, P.B., Chu, D., Tong, J. Sun, Y., Song, H., He, W. and Tian, L., 2014, Anoxia/high temperature double whammy during the Permian-Triassic marine crisis and its aftermath: Scientific Reports, v. 4, p. 1-7, doi:10.1038/srep04132.

Thompson, J.R., Petsios, E., Davidson, E.H., Erkenbrack, E.M., Gao, F., and Bottjer, D.J., 2015, Reorganization of sea urchin gene regulatory networks at least 268 million years ago as revealed by oldest fossil cidaroid echinoid: Scientific Reports, v. 5, p. 1-9, doi:10.1038/srep15541.

Yuan, D.X., Shen, S.Z., Henderson, C.M., Chen, J., Zhang, H., and Feng, H.Z., 2014, Revised conodont-based integrated high-resolution timescale for the Changhsingian Stage and end-Permian extinction interval at the Meishan sections, South China: Lithos, v. 204, p. 220–245.